Ocean Engineering 278 (2023) 114310

Contents lists available at ScienceDirect

Ocean Engineering

journal homepage: www.elsevier.com/locate/oceaneng

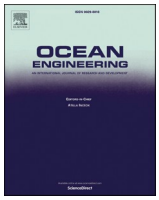

Design of a novel energy harvesting mechanism for underwater gliders using thermal buoyancy engines

Hongbo Hou [a], Abel Arredondo Galeana [a], Yang Song [b], Gang Xu [c], Yunxin Xu [a], Weichao Shi [a,*]

[a] Department of Naval Architecture, Ocean & Marine Engineering, University of Strathclyde, UK
[b] School of Mechanical Engineering, Tianjin University, Tianjin, China
[c] School of Naval Architecture and Ocean Engineering, Jiangsu University of Science and Technology, Zhenjiang, China

ARTICLE INFO

Handling Editor: Prof. A.I. Incecik

Keywords:
Energy harvesting mechanism
Underwater glider
Thermal buoyancy engine
Turbine optimization
BEMT

ABSTRACT

Underwater gliders (UGs) are becoming popular in ocean exploration. However, the main limitation for their development is their supply of energy. This paper proposes a novel energy harvesting mechanism for an underwater glider equipped with a thermal buoyancy engine. The thermal buoyancy engine changes the buoyancy of the glider, due to the difference of temperature of the ocean, and it drives the glider up and down in the water. These manoeuvres drive a turbine behind to harvest energy. Based on this harvesting mechanism, first, a new type of thermal buoyancy engine with high ballast capacity is presented. Secondly, a dedicated turbine, mounted behind the glider, is optimally designed based on the Blade Element Momentum Theory (BEMT). In order to consider the un-uniform inflow generated by the wake of the glider, an upgraded version of the BEMT model has been developed. With the results obtained in this paper, enhanced energy efficiency for a self-sustainable underwater glider can be achievable.

1. Introduction and background

Oceans play an increasingly important role in the global economy. Hence, ocean monitoring is crucial to expand our knowledge and protect the wealth of oceans (Falcão Carneiro and Gomes de Almeida, 2018). For centuries, oceanographers relied on ships to get data and make observations during the cruise. In fact, a body of knowledge, that involves ocean circulation, plate tectonics, global ocean productivity, climate-ocean coupling, etc., was gathered through ship observation (Schofield et al., 2007). However, ships cannot provide sufficient spatial and temporal resolution. Furthermore, they incur in very high operating costs. Therefore, underwater gliders (UGs) have become one of the major alternatives in ocean exploration because of their low operational cost.

Gliders, in contrast to ships, have a more limited payload capacity. Hence, it is important to design energy efficient gliders that can operate long hours in the ocean. Hence, in this work, we present a glider that is powered by a buoyancy engine, which can generate a buoyancy change to drive the glider up and down in the water. As the glider ascends or descends, the hydrofoils of the hull control the angle of ascend/descend, allowing the UG to move in a sawtooth trajectory, as shown in Fig. 1.

Companies and organizations have already developed several commercial UGs with electrical buoyancy engines, such as Slocum, Seaglider (Eriksen et al., 2001), Spray (Sherman et al., 2001) and Petrel (Xue et al., 2018). To extend the operation of gliders in the ocean, the use of ocean thermal energy to drive a thermal buoyancy engine in a glider has been proposed as a solution (Wang et al., 2020; Webb et al., 2001; Yang et al., 2016; Ma et al., 2016). As an alternative to the electrical buoyancy engine that relies on battery power, the thermal buoyancy engine can harvest thermal energy of the ocean to increase the voyage of the glider by 3–4 times (Davis et al., 2002b). For example, the pioneering Slocum glider, developed by Webb Research Corporation and equipped with a thermal buoyancy engine, covered a distance of 40,000 km (Webb et al., 2001).

However, thermal gliders are still limited by the battery power which provides energy for their onboard payloads and attitude control systems. Furthermore, both electrical and thermal gliders are limited by low speeds, with maximum speeds of 1knot, which often requires additional thrusters if high-speed cruising is required. Therefore, for a thermal glider, it would be ideal to convert thermal to electrical energy, to assist with the electrical payload of the glider. Current technologies focus on hydraulic-based systems, which use a mini generator in the high-

* Corresponding author. Department of Naval Architecture, Ocean & Marine Engineering, University of Strathclyde Henry Dyer Building, 100 Montrose Street, Glasgow, G4 0LZ, UK.
E-mail address: weichao.shi@strath.ac.uk (W. Shi).

https://doi.org/10.1016/j.oceaneng.2023.114310
Received 31 July 2022; Received in revised form 20 March 2023; Accepted 22 March 2023
Available online 5 April 2023

pressure oil pipeline to recover energy during the ballasting and de-ballasting stages when the thermal engine is pumping hydraulic oil. In 2016, the technology, SOLO-TREC, was developed based on this principle (Chao, 2016). The Teledyne Webb Research consortium built the Slocum Thermal E-Twin engine, with a similar energy harvesting system for gliders (Jones et al., 2014). Tianjin University also developed the OTEC-PCM engine, based on a similar operating principle (Wang et al., 2019). The advantage of this hydraulic energy harvesting system is that it is simple and compact. The disadvantage is that it is limited in energy output. For example, the energy yield of the Slocum-TREC glider with 10 kg phase change material (PCM) is around 6.5 kJ per working cycle when the working depth is 1200m (Haldeman et al., 2015a). Furthermore, the hydraulic generator runs at high pressure with a low volume oil circuit which results in low efficiency and high failure rate.

Therefore, this research proposes a new-type ocean thermal energy harvesting mechanism that can be applied to UGs aiming for high energy yield. The mechanism uses a thermal buoyancy engine and a foldable turbine. The latter is mounted behind the hull of the glider.

In this work, when the glider is in power-generation mode, the thermal buoyancy engine uses the thermal energy to change its buoyancy and drive the glider vertically with the assistance of an attitude adjustment unit. During the ascend and descend, the foldable turbine behind the hull opens and harvests energy. To maximize the power output of the energy harvesting system, this study designs a new-type of thermal engine with high ballast capacity in order to provide a large driving force. Followingly, this study develops a mathematical model based on Blade Element Momentum Theory (BEMT) to design and optimize the turbine geometry. The mathematical model can also be used to estimate the capacity of the energy harvesting system. The model shows that when the glider uses the new-type of thermal engine and runs with the optimized turbine, the energy harvested is about 24.2 kJ of energy per descent-ascent cycle. This is considering a working depth of 1000 m. Noteworthy, 24.2 kJ of energy can support the energy consumption of the glider in about 4 descent-ascent cycles (Falcão Carneiro and Gomes de Almeida, 2018).

Hence, the main purpose of this paper is to introduce the principle and the optimization method of the novel energy harvesting mechanism, demonstrate the effectiveness of this mechanism at the hydrodynamic level, and find the design philosophy of the turbine in this energy harvesting mechanism. This paper is organized as follows. Section 1 presents the introduction. Section 2 introduces the concept of power generation through the turbine. Section 3 introduces the design of the novel thermal buoyancy engine. Section 4 describes the design and optimization of the turbine based on BEMT by constructing a mathematical model. Section 5 analyzes the results of the mathematical model. Finally, Section 6 concludes this study by summarizing the main conclusions drawn in this work.

2. Design for energy efficiency and energy harvesting

As mentioned above, this research proposes a new-type of energy harvesting mechanism. Hence, the UG is designed to have two operating modes: the gliding mode and the energy harvesting mode.

In the gliding mode, the UG is driven by the thermal buoyancy engine and moves in a saw-tooth trajectory (see Fig. 2). In this condition, the thermal buoyancy engine uses part of its ballast capacity to glide in an energy-efficient manner. To minimize the resistance, the energy harvesting turbine is folded behind the hull of the glider, as shown at the inset of Fig. 2.

When the UG turns into energy harvesting mode, the thermal buoyancy engine harvests thermal energy and use its maximum ballast capacity to drive the UG at maximum speed. The motion of the UG is perpendicular to the water surface with the assistance of an attitude adjustment unit. In this operating mode, the foldable turbine unfolds and spins under the drive of the fluid to harvest energy, as shown in Fig. 3.

Note that the efficiency of the thermal buoyancy engine and the turbine directly affects the amount of energy that is harvested. Therefore, improving both the operation of the engine and the turbine are key to the success and usefulness of this technology.

3. Thermal buoyancy engine for energy harvesting

The temperature of seawater drops rapidly from 20 to 30 °C to generally 4 °C when the water depth exceeds 200 m due to the ocean's thermocline (Kong et al., 2010). The temperature difference between the sea surface and deep water creates thermal energy in the ocean (Ma et al., 2016). The thermal buoyancy engine is a device that can harvest ocean thermal energy through a phase change material (PCM). The engine uses thermal energy and the properties of the PCM, to change its buoyancy and to drive the UGs up and down (Yang et al., 2016; Javaid et al., 2014).

Because the thermal engine drives the energy harvesting system, i.e. the turbine, the engine determines the upper limit of the harvestable

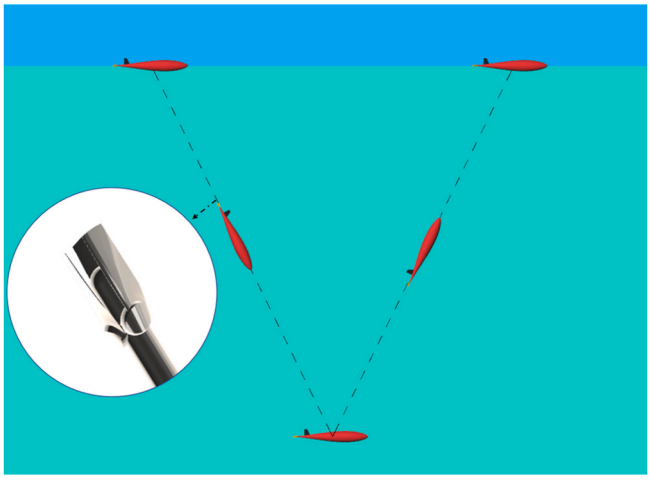

Fig. 2. The gliding mode.

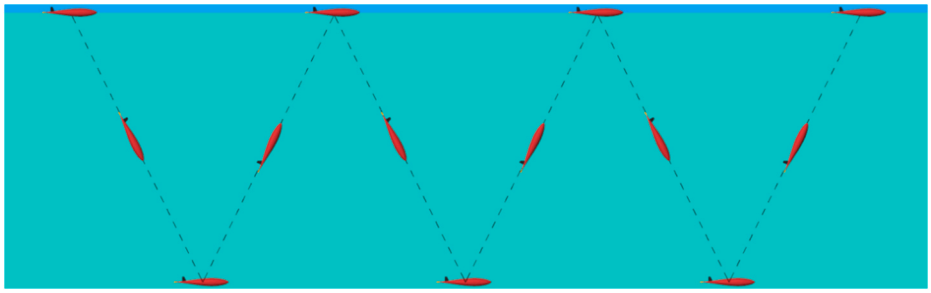

Fig. 1. The sawtooth trajectory of an UG.

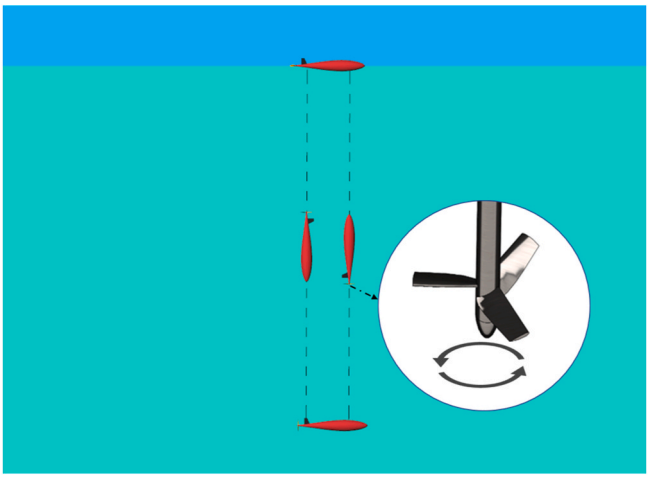

Fig. 3. Energy harvesting mode.

kinetic energy. The traditional thermal buoyancy engine design is tailored to provide the UG the ability to glide rather than to harvest energy. Hence, the engine is generally designed to have a small ballast capacity. In this paper, in order to provide more kinetic energy to the energy harvesting turbine, a conceptually new-type of thermal buoyancy engine is proposed to increase the ballast capacity without increasing the volume of PCM. The traditional thermal buoyancy engine and the new concept are introduced in the following sections.

3.1. Traditional thermal buoyancy engine

Fig. 4 shows the schematic of the traditional thermal engine system. The engine has two chambers referred to as Chamber 1 and Chamber 2. Chamber 1 is the heat transfer unit. In this chamber, the working fluid is the phase change material (PCM). The PCM expands and squeezes hydraulic oil into Chamber 2, as it harvests thermal energy and melts. Chamber 2 is a mechanical energy storage accumulator with high-pressure gas, usually nitrogen ($N2$).

The working cycle of the thermal engine can be divided into four main steps. In step 1, when the UG is on the sea surface, the PCM in Chamber 1 starts to melt and expand. As it expands, it squeezes oil from the heat transfer unit into the accumulator. The check valve prevents backflow of the oil.

In step 2, the oil in the external bladder is squeezed into the inner bladder by the atmospheric pressure when the 3-way valve opens. Then, the buoyancy decreases, resulting in the descent of the UG. With the increase of the diving depth, the temperature falls rapidly. The liquid PCM in the heat transfer unit starts to solidify and contracts. This contraction causes the oil in the internal bladder to flow into the heat transfer unit.

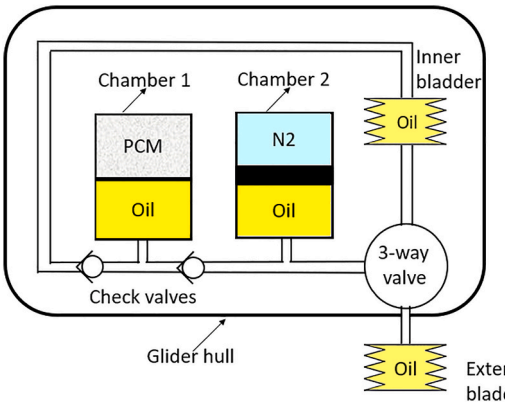

Fig. 4. Schematic of the traditional thermal engine system (Webb et al., 2001).

In step 3, the UG reaches the target depth, the 3-way valve opens and the oil in the accumulator is pushed into the external bladder. Then, the buoyancy increases, and the AUV starts ascending. Lastly, in step 4, the AUV reaches the sea surface and the next cycle starts (Webb et al., 2001).

The advantage of this type of heat engine is its simple structure and reliability. However, its disadvantage is that the ballast force is very limited. For example, the Slocum thermal E-twin with two heat transfer units provides only about 1000 cc of working pressurized oil. This is equivalent to 10 N of buoyancy force (Jones et al., 2014). The reason is that the PCM mass is limited and its expansion rate is low. In this work, the limited ballast force offered by the traditional thermal engine cannot provide the turbine behind the hull with enough kinetic energy to extract energy.

3.2. The new-type buoyancy engine

To provide more kinetic energy to the turbine in the energy harvesting mode, we propose a new-type of thermal buoyancy engine. A patent for the engine has been applied. The new engine amplifies the ballast capacity without increasing the mass of the PCM (Shi et al., 2022). The principle of the new-type of buoyancy engine of this paper is to take full advantage of the high pressure that the PCM can generate.

In a traditional buoyancy engine, the working pressure of the PCM is very low compared to the pressure that the melting PCM can generate. The required working pressure of the PCM in the traditional thermal engine is only slightly higher than the working pressure of the UG in deep-sea which is normally 10 MPa. The highest pressure of melting PCM or nitrogen in the accumulator is 11–12 MPa (Ma et al., 2016).

However, the maximum pressure generated by melting PCM can be much higher than the working pressure of the UG. For example, the volumetric expansion rate of paraffin wax can reach 9% in the phase change process when the pressure is 60 MPa (Klintberg et al., 2002). When the n-pentadecane is used as PCM in the heat transfer unit, the highest thermodynamic efficiency will be obtained when the working pressure reaches 90 MPa (Falcão Carneiro and Gomes de Almeida, 2016). This shows that the pressure of the melting PCM in the heat transfer unit is too low for the PCM to release all its potential power and working efficiency for the thermal engine.

Inspired by the above property of the PCM, in this work, a conceptually new-type of thermal engine is proposed to fully use the high pressure that the PCM can generate. This will amplify the ballast capacity of the buoyancy engine.

The workflow of the thermal engine consists of 2 steps. The first step is to increase the pre-charge pressure (P_P) of the gas in the accumulator according to the thermodynamic properties of the PCM. The high working pressure will enable the PCM to work with high thermodynamic efficiency.

The second step is to use a hydraulic pressure transfer cylinder which is shown in Fig. 5 to convert the high pressure in the accumulator to low working pressure in the external bladder for greater ballast capacity. This assembly consists of a high-pressure double-acting cylinder with a small cross-sectional area, a low-pressure single-acting cylinder with a large cross-sectional area, and a hydraulic rod connecting the pistons in the two cylinders.

When the piston in the hydraulic pressure conversion unit is pushed to move by the oil from the accumulator, the high oil pressure in the double-acting cylinder will be transferred to low oil pressure in the single-acting cylinder, the intake of oil volume in the high-pressure cylinder is amplified in the low-pressure cylinder because of the increase in cross sectional area. In other words, the hydraulic pressure transfer cylinder is a buoyancy amplifier for the thermal buoyancy engine. The buoyancy magnification (M_b) is the ratio between the cross-sectional area of the low-pressure cylinder (A_l) to that of the high-

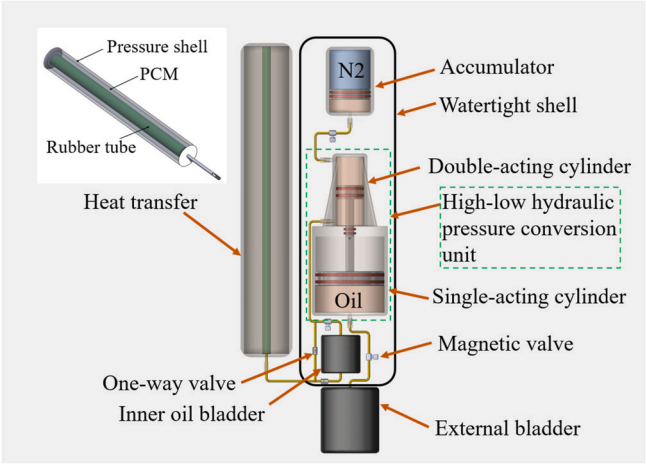

Fig. 5. The schematic of the new-type thermal buoyancy engine.

pressure cylinder (A_h). With the same amount of PCM, the new-type of buoyancy engine can amplify the buoyancy change by a factor of M_b. This will provide more kinetic energy to the turbine. The schematic of the new-type of thermal buoyancy engine is shown in Fig. 5.

4. Design and optimization of the turbine

The turbine is used for converting kinetic energy, due to the motion of the glider, into dynamic output and electricity. Hence, the geometry of the turbine determines the efficiency of the system. To design and optimize a turbine geometry for maximizing the energy yield, this paper develops a mathematical model based on Blade Element Momentum Theory (BEMT). The mathematical model is also used to estimate the energy harvesting capacity of the system. Before introducing the mathematical model computations, the traditional BEMT method is modified to accommodate the wake of the glider as inflow condition, as well as to incorporate the effect of the Reynolds number (Re) in the turbine.

4.1. Modified BEMT in this paper

4.1.1. The principle of traditional BEMT

Although computational fluid dynamics (CFD) has experienced significant development in the last few decades and has higher fidelity, it is still costly in terms of computational resources and time (Liu and Janajreh, 2012). In comparison with computational fluid dynamic (CFD) of underwater turbines, although the accuracy of the BEMT code might be lower to predict the loading on the turbine, it still a useful tool to determine the optimal turbine geometry and operating conditions (Khchine and Sriti, 2017). Most importantly, the time and computational cost of BEMT is much lower than the CFD method.

The Blade Element Momentum Theory (BEMT) combines blade element theory and the momentum theory. The blade element theory divides the turbine blade into several individual segments. This assumes that forces acting on the blade segments are only determined by the lift and drag coefficients of the foil cross-section (Bangga et al., 2018). The momentum theory is used to calculate the change of flow momentum and angular momentum around the blade. The changes in axial and angular momentum are equated to the computed blade element thrust and torque, respectively. Then, the loads on the blades are calculated (Liu and Janajreh, 2012). The BEMT is based on the assumptions of steady, inviscid, incompressible flow without radial and circumferential dependency (Sultania and Manuel, 2010). Since these assumptions lead to accuracy problems, some corrections are used in practical application to obtain solutions with higher fidelity (Manwell et al., 2010), such as tip loss correction (Shen et al., 2005), 3D correction (Chaviaropoulos and Hansen, 2000), etc.

The BEMT can be used to design a turbine, like the one used in the UG of this work. The velocity triangle on a section of the blade in the frame of reference of the turbine is shown in Fig. 6. In the figure, U_∞ is the inflow velocity of the freestream. W is the relative velocity, α is the angle of attack of foil, β is the twist angle of blade element, $\varnothing$ is the inflow angle, a is the axial induction factor which indicates the fractional drop in axial flow velocity between the freestream and the turbine rotor, a' is the tangential induction factor which indicates the fractional increase in tangential flow velocity. Here, we use λ to define the tip speed ratio, which is the ratio of the turbine tip velocity to U_∞, R is the radius of the turbine and r is the local radius of the blade element.

According to BEMT, a turbine will reach its maximum efficiency when the a is $\frac{1}{3}$ because the highest extractable power for a turbine can be achieved by reducing the flow velocity through the turbine plane to two-thirds of its upstream value (Manwell et al., 2006). With the optimal a, a' can be calculated with Eq. (1)., such that

$$a' = \frac{a(1-a)}{\lambda_{design}{}^2 \mu^2} \quad \text{Eq. 1}$$

where the λ_{design} is the design tip speed ratio which is the optimal operating TSR desired at the design stage. In Eq. (1), μ is the ratio of the local radius of a blade element to the total radius ($\frac{r}{R}$).

Once a and a' are known, $\varnothing$ is calculated with Eq. (2), such that:

$$\tan\varnothing = \frac{1-\mathrm{a}}{\lambda_{\mathrm{design}} * \mu(1+\mathrm{a}')} \quad \text{Eq. 2}$$

Then, β is calculated with Eq. 3

$$\beta = \varphi - \alpha \quad \text{Eq. 3}$$

Then, the torque at each sectional radius calculated with blade element theory is equated to the torque calculated with momentum theory. This relationship yields Eq. (4), such that:

$$C = \frac{8\pi\lambda_{design}\mu^2 a'(1-\mathrm{a})RU_\infty^2}{N(C_L\, sin\varnothing - C_d\, cos\varnothing)W^2} \quad \text{Eq. 4}$$

where C is the optimal chord length, C_L is the lift coefficient, C_d is the drag coefficient, N is the blade number. Using Eq. (4), the optimal chord length can be calculated.

In this paper, we also use BEMT to analyse the hydrodynamic performance of a turbine. The analysis part of BEMT uses iteration to determine the a and a' of the blade element to calculate the load on the foil. At the start of the iterations, a and a' are set to zero as the initial condition. Then the inflow angle (φ) is calculated by Eq. (2) replacing λ_{design} with the operating tip speed ratio ($\lambda_{operating}$). Then, by Eq. (3), the angle of attack (α) is calculated which is used to find the C_L and C_D for each foil segment. Subsequently, the normal coefficient (C_n) and the tangential coefficient (C_t) of each foil segment is calculated with Eqs. (5) and (6), such that.

$$C_n = C_L\, cos\varnothing + C_D\, sin\varnothing \quad \text{Eq. 5}$$

and

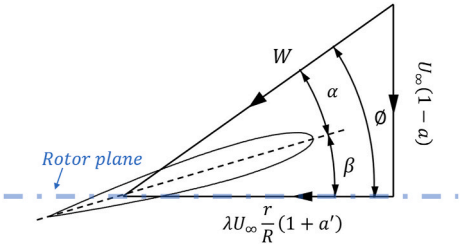

Fig. 6. Velocities relating to the turbine blade.

$$C_t = C_L\, sin\varnothing - C_D\, cos\varnothing \quad \text{Eq. 6}$$

Then, the chord solidity (σ_r)is calculated by Eq. 7

$$\sigma_r = \frac{N * C}{2 * \pi * \mu * R} \quad \text{Eq. 7}$$

Where N is the blade number.

With C_n and C_t, the axial and tangential induction factor are determined using the Eqs. (8) and (9).

$$a = \frac{1}{\frac{4\ sin^2\ \varphi}{\sigma_r C_n} + 1} \quad \text{Eq. 8}$$

$$a' = \frac{(1-a)\sigma_r C_t}{4\lambda_{operating}\mu\ sin^2\ \varphi} \quad \text{Eq. 9}$$

Then, the calculation replaces the previous a and a' with the newly calculated a and a' and the procedure is restarted. The iteration stops when the residual of a and a' is less than 0.01.

Once the iteration procedure is completed, the torque (δT_{or}) and the thrust (δT_h) for each blade element is evaluated using the Eqs. (10) and (11), such that.

$$\delta T_{or} = \frac{1}{2} * \rho * W^2 * N * C * r * C_t * \delta r \quad \text{Eq. 10}$$

$$\delta T_h = \frac{1}{2} * \rho * W^2 * N * C * C_n * \delta r \quad \text{Eq. 11}$$

where C_t and C_n are the result of iteration.

Considering the idealization of the BEMT, there are several kinds of common corrections to the BEMT analysis in real application. Including the tip loss correction (Shen et al., 2005), turbulent wake state correction (Buhl, 2005), and 3D correction (Chaviaropoulos and Hansen, 2000).

4.1.2. BEM model validated versus experimental literature data

We present a validation of the BEM model versus experimental data available in literature. We consider the experimental data from Shi et al. (2019). The experimental data shows the Cp and Ct curves of a pitch-adjustable tidal turbine with a radius of R = 0.2 m. The blade section consists of a S814 section profile. The geometry of the turbine is shown in Fig. 7, the chord length and twist angle of cross sectional sections of the blades, located at r/R, are shown in Table 1.

The experiment was carried out at a basically constant *Re* number (142000–170000). The test was conducted in the towing tank of the Kelvin Hydrodynamic Lab (KHL). Further details of the test and facility are available in (Shi et al., 2019). The uncertainty level of the experiment was 0.3% for the TSR, 1.1% for the Cp and 0.2% for Ct/10 which were computed statisfically, based on 7 individual tests at TSR = 4 (Shi et al., 2019).

Fig. 7. The turbine in the experiment (Shi et al., 2019).

The details of the turbine and of the experimental conditions are imported into, the hydrodynamic BEMT code. Hence, the Reynolds number (*Re*) considered in our simulation is the same as that of the experiment. Then, the hydrodynamic performance of the turbine is analyzed at different TSRs. Figs. 8 and 9 show the comparison between experiment and BEMT simulation. It can be seen that a satisfactory agreement (generally under 5% difference) is achieved. Some high discrepancies appear in the low TSR region as the turbine is experiencing stall. This is because the BEMT code based on Xfoil simulation can not predict the stall accurately. But as the following research is mainly focusing on the maximum efficiency, BEMT shows great accuracy in predicting the turbine performance.

4.1.3. Modifications to traditional BEMT

Different from the conventional applications of BEMT with uniform free stream conditions, the working condition of the turbine in this study has two characteristics. The first one is that all the blade elements work in a strong wake behind the hull. The second one is that the blade elements may work at low Reynolds number (*Re*) range which is less than 50,000 in some cases. These two characteristics will influence the design of the turbine. To account for the two special working conditions, this work modifies the BEMT for both wake and Reynolds numbers. Although the modifications will alter the results of the traditional BEMT model, the core of the model remains the same, and results are expected to be a valid physical representation of a turbine operating behind the wake of a glider. We explain the modified BEMT model in the next sections.

4.1.3.1. Modification for wake behind the hull. The traditional BEMT assumes that the incoming flow velocity is uniform, while the incoming flow in this work is the wake of the UG hull, whose velocity is non-uniform. This non-uniform velocity will render the traditional BEMT uniform flow assumption invalid and lead to some inaccurate predictions. For example, with the non-uniform incoming flow, the design angle of attack (α) of the blade element at which the foil has optimal hydrodynamic performance changes, and the traditional BEMT model does not account for this change.

To adjust the BEMT model for non-uniform inflow conditions, this work modifies the BEMT inflow based on a CFD simulation of the wake behind the UG hull. Results are shown in Fig. 7(a). We note that the thermal engine can be made into an interlayer-type to avoid influencing the shape of the UG (Zhang et al., 2009). Therefore, the CFD simulation does not consider any geometric influence of the thermal engine. The wake distribution located at 5% of the hull length (L) downstream of the UG is shown in Fig. 10. Fig. 10(a) shows the *zx*-plane, showing a top view of the glider. Fig. 10(b) shows the *xy*-plane, showing the back view of the glider.

As shown in Fig. 7(b), the wake is approximately axial symmetric. This is because the wings of the UG have a reduced influence on the wake. Hence, we assume a symmetric wake, as highlighted with the dot-dash lines in Fig. 10(b). We note that changes in wake distribution caused by the interaction between hull and turbine are not considered in this work. Hence, under these assumptions, the inflow velocity distribution in front of the turbine is shown in Fig. 11(a). The velocities on a section of the blade, located in plane A-A, in the frame of reference of the turbine is shown in Fig. 11(b). Note that plane A-A is also indicated in Fig. 11(a).

In Fig. 11(b), W_f is the wake factor expressed by Eq. (12), such that

$$W_f = \frac{V_{wake}}{U_\infty} \quad \text{Eq. 12}$$

where the U_∞ is the incoming velocity.

Table 1
The detailed geometry of the turbine.

r/R	0.2	0.3	0.4	0.5	0.6	0.7	0.8	0.9	1
Chord length (mm) (mm)	64.4	60.1	55.8	51.5	47.2	42.9	38.6	34.3	30
Twist angle (deg)	27	15	7.5	4	2	0.5	−0.4	−1.3	−2

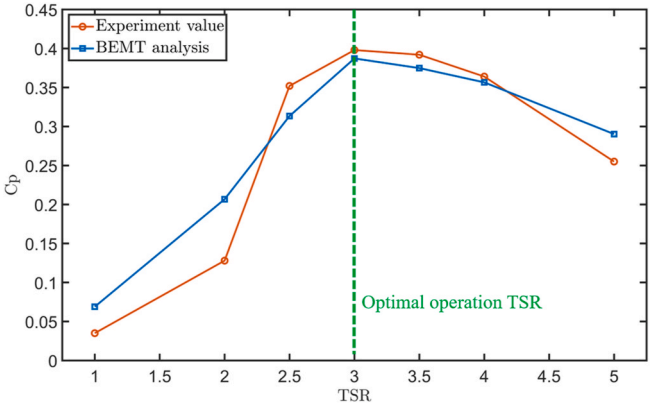

Fig. 8. The C_p of the expriment value and the BEMT analysis.

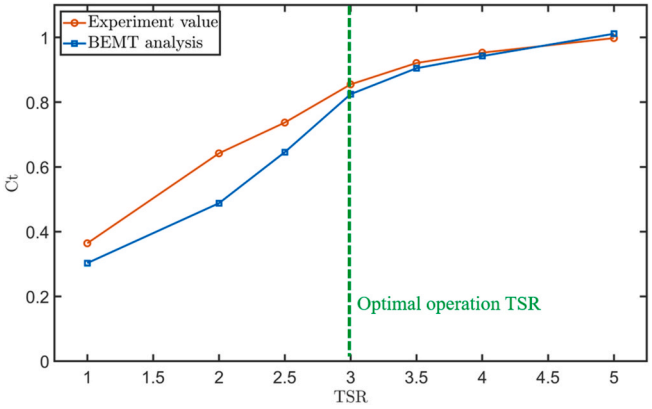

Fig. 9. The C_t of the expriment value and the BEMT analysis.

Then, $\lambda_{equivalent}$ in Fig. 11(b), can be expressed by the Eq. (13), such that

$$\lambda_{equivalent} = \frac{\lambda}{W_f} \quad \text{Eq. 13}$$

Comparing Figs. 11(b) and Fig. 6, we note that the blade elements behind the wake operate at $\lambda_{equivalent}$. So, in the BEMT design process shown from Eq. (1) to Eq. (4), λ_{design} is converted to $\lambda_{equivalent}$ with Eq. (13). This allows us to recalculate the twist angle and chord length for the turbine behind the glider. In the BEMT analysis, denoted from Eq. (4) to Eq. (9), the $\lambda_{operating}$ is also converted into $\lambda_{equivalent}$ with Eq. (13). Hence, we can recalculate $\varnothing$, α, a, a'. Finally, W in the wake is calculated and used to determine the real power and thrust of the turbine.

This modification can eliminate the influence of wake on the pre-assumptions of the traditional BEMT, allowing BEMT to work properly in the special operating conditions of this work.

4.1.3.2. Modification for low Reynolds number. In the design and analysis part of traditional BEMT, the lift coefficient (C_L) and the drag coefficient (C_D) curves do not consider the influence of a varying Reynolds number (Re) on the turbine hydrodynamic performance. In this work, this approach may no longer be appropriate. Considering the low moving speed of the whole system and the influence of the wake, the turbine blades sometimes work at low Re ($Re < 50{,}000$). In this range, the hydrodynamic performance of the blade element deteriorates and is sensitive to Re (Deters et al., 2014; Li, 2013). To consider the influence of Re we show the influence of Re in the Cl/Cd ratio versus α of a NACA 0015. The ratio is plotted as a 2-D contour plot in Fig. 12. In the figure, α ranges from 0 to 17°, in the vertical axis, and Re ranges from 10.000 to 170,000, in the horizontal axis. The functions of C_L and C_D in this work are obtained by calculating and interpolating the hydrodynamic performance of the NACA 0015 under different Re and α with the software Xfoil. Fig. 12 shows that the Cl/Cd ratio drops as the Reynolds number decreases. Hence, it is an important consideration in our modified BEMT model.

In the design part, the geometry of the turbine is unknown, and so is Re. In this work, we use an iteration procedure to determine Re and the

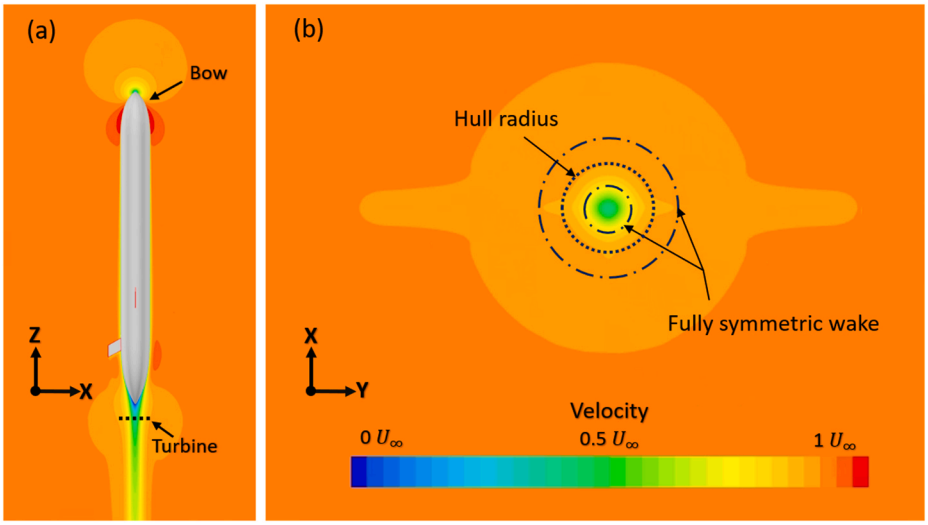

Fig. 10. The typical wake distribution behind the UG.

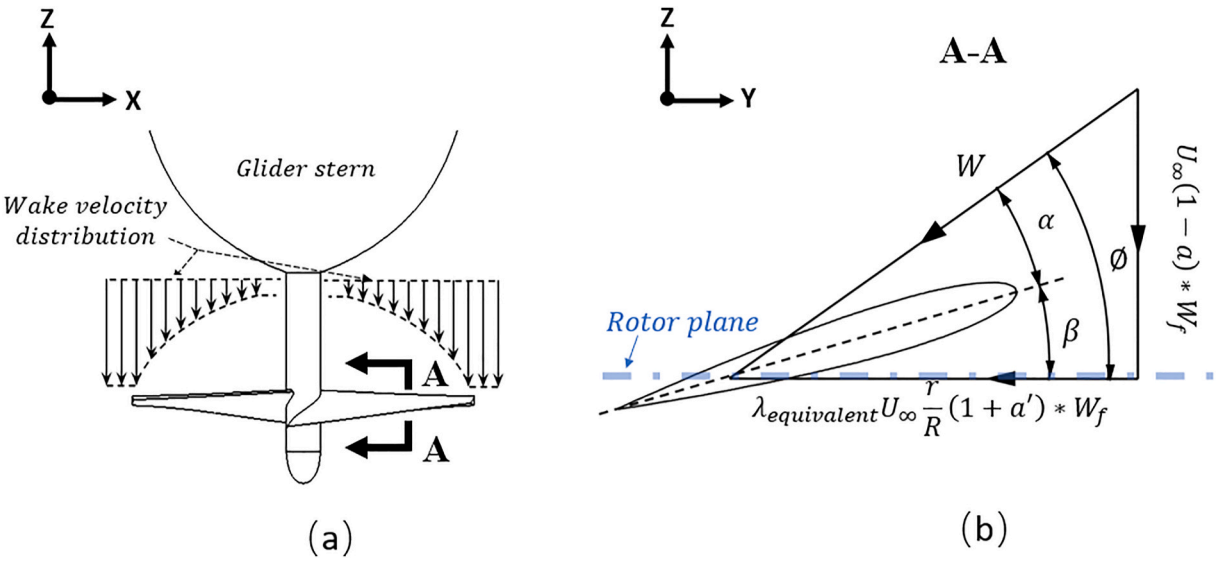

Fig. 11. Velocities relating to the turbine blade in wake a) the side view b) the foil section view.

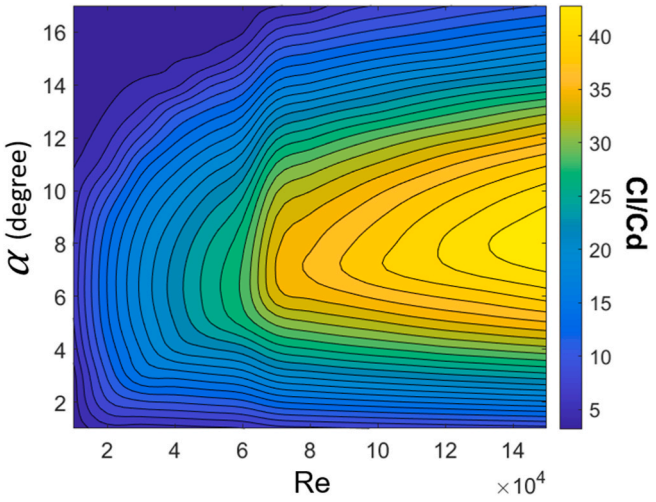

Fig. 12. The lift-to-drag ratio of NACA 0015.

final geometry of the blades of the turbine based on BEMT.

The design process is shown in Fig. 24 in appendix A. At the start of the process, a, R, λ_{design}, and W_f are provided as the input to the modified BEMT code. Then, $\lambda_{equivalent}$ is calculated with Eq. (13). This $\lambda_{equivalent}$ is used to replace the λ_{design} in the traditional BEMT, when calculating the $a^{'}$ and the chord length (C). After calculating $a^{'}$, the inflow angle ($\varnothing$) and the twist angle (β) are calculated with Eq. (2) and Eq. (3), respectively. Then, the relative velocity W, shown in Fig. 11(b), is calculated. Then, we input the C_L and C_D functions of Re. Next, an initial Re which is set as 100,000 is used to start the iteration. The C_L and C_D is recalculated according to the Re that results from the iteration. With C_L and C_D, the chord length is calculated with Eq. (4). Since the chord length in the loop has been determined, the new Re can be calculated. The iteration continues until the residual of Re is below 1000 which can only cause very marginal foil hydrodynamic change even when the Re is very low.

4.1.3.3. Benchmarking the modified BEMT model. In this Section, we compare the modified and unmodified BEMT models.The modified BEMT model analyses the turbine operating behind the wake of a hull. Hence, the turbine experiences a nonuniform inflow and a low Re near the hub caused by the concave shape of the wake (see Fig. 10(a)). The result of the comparison are shown in Figs. 13 and 14. It can be seen that both the C_p and C_t drop approximately by up to 16.5% and 7%.

The drop of C_p qualitatively similar to the results of a wind turbine located in the second row of an wind farm array (Barthelmie et al., 2009). This provides confidence, that the modified BEMT model shows in fact physically realistic data, and accounts for the effect of a turbine operating behind a blockage, in this case the hull of the UG.

The drop of turbine performance, in the modified BEMT model, is caused by three main reasons. Firstly, due to the deficit in wake energy. Secondly, due to the lower Re number behind the wake as opposed to the Re number in open water. Lastly, and thirdly, the difference between turbine design conditions (open water) and working conditions (wake), which modifies the angle of attack of the blade elements. We quantiy the first effect, the energy deficit E_d, as follows. We divide the area within the radius of the turbine into 500 equal-width rings of different radiuses. Then, the energy on each ring is computed and added. Hence, the energy deficit can be defined with Eq. (14), such that:

$$E_d = 1 - \frac{\sum_{i=1}^{500} \frac{1}{2}\rho\left(U_\infty * W_{f_i}\right)^3 2\pi r_i * \Delta r}{\frac{1}{2}\rho U_\infty^3 \pi R^2} \quad \text{Eq. 14}$$

where the W_{f_i} is the wake factor of the i th ring, the r_i is the radius of the i th ring. Δr is the wide of each ring ($\frac{R}{500}$).

Behind the hull, E_d is around 13%, which is similat to the estimated

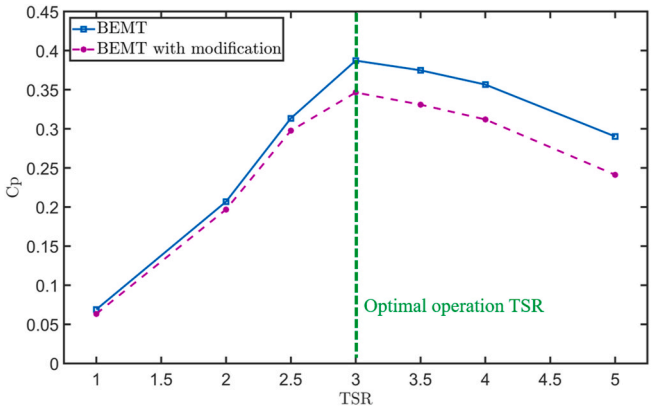

Fig. 13. The C_p in the BEMT with and without modification.

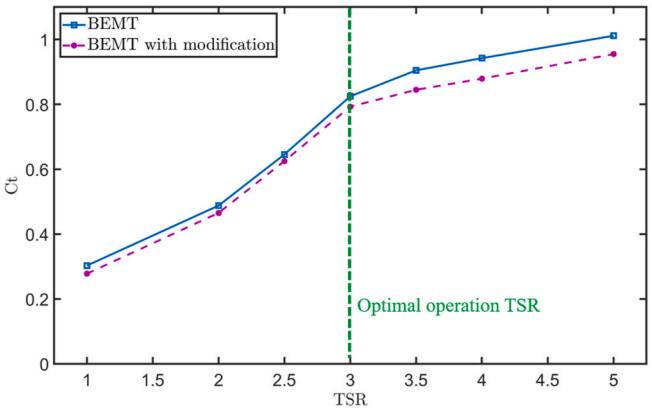

Fig. 14. The C_t in BEMT with and without modification.

power drop of Fig. 13 (approximately 16.5%). Therefore, it can be seen that the drop of C_p is mainly due to the drop of energy available in the wake. The lower *Re* caused by wake and the not ideal angle of attack of some blade elements can influence the hydrodynamic performance of the turbine, but their effect does not seem to be that significant.

4.2. Design considerations of the UG

In this section, we present some of the design considerations for the UG as the preconditions for the mathematical model to design the geometry of the turbine for optimum energy extraction. The detailed flowchart of the mathematical model is introduced in the following section. Prior to introducing this flow chart, we describe four steps that are considered, as part of the design considerations of the UG.

Step 1 : Input the working environment of the UG. In this case, the working depth of the UG (d_w) is 1000 m, the water temperature at the surface (T_h) is 28 $^\circ C$, the water temperature at working depth (T_l) is 4 $^\circ C$, (Ma et al., 2016). At d_w, the working pressure of the UG ($P_{working}$) is approximately 10 Mpa which is the hydrostatic pressure at a depth of 1000 m.

Step 2: Input the information about the UG hull. In this case, a typical UG hull geometry is chosen. The UG length (L) is 2 m, and the radius (R_g) is 0.095 m, as shown in Fig. 15.

Then, the wake distribution and the resistance of the hull from the CFD STAR CCM + simulation is input into the mathematical model in function form. The radial wake distribution, located 0.05 L downstream of the UG, is expressed by the wake factor (W_f) in Eq. (15). Since the wake distribution varies limitedly with cruising speed, it is considered to be independent of the cruising speed, and only dependent on the radial coordinate r. The relationship between hull resistance (R_h) and cruising velocity V can be expressed with Eq. (16).

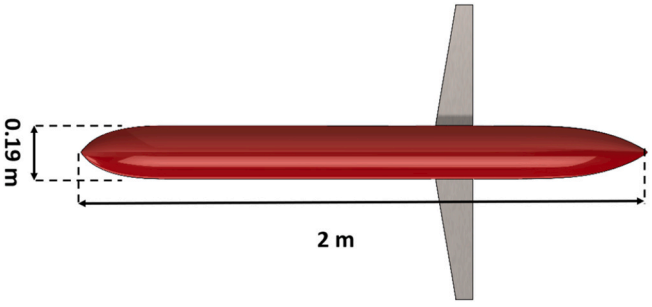

Fig. 15. The geometry of the UG in this study.

$$W_f = -0.0161r^4 + 0.3652r^3 - 1.2394r^2 + 1.5293r + 0.32 \quad \text{Eq. 15}$$

$$R_h = 2.0681V^2 + 1.2188V - 0.279 \quad \text{Eq. 16}$$

Step 3: Input the information about the thermal buoyancy engine. There are two assumptions about the thermal engine in the mathematical model: (a) The hydraulic components are considered ideal. (b) The temperature of N_2 in the accumulator is considered constant. The PCM in the engine in this case is n-Pentadecane whose PVT relationships, which relate pressure(P), volume(V), and temperature (T) of the PCM, are expressed with Eq. 17a-b (Falcão Carneiro and Gomes de Almeida, 2016), such that (Falcão Carneiro and Gomes de Almeida, 2016):

$$V_{PCM_S} = 1.198 - \left(\frac{1}{55}\right)(P_{PCM} * 0.0143 - 0.0408 * (T_{PCM} + 5.5)) \quad \text{Eq. 17(a)}$$

$$V_{PCM_L} = 1.3195 - \left(\frac{1}{300}\right)(P_{PCM} * 0.1817 - 0.2733 * (T_{PCM} - 30)) \quad \text{Eq. 17(b)}$$

where the V_{PCM_S}, V_{PCM_L} are the volume of PCM in solid, and liquid phases respectively.

The volume of PCM (V_{pcm}) is 12 L (about 9.7 kg) in solid phase which is compatible with the payload capacity of existing UGs (Falcão Carneiro and Gomes de Almeida, 2016). The pressure in the hull (P_{inner}) is set as 0.1 Mpa. The maximum gas pressure in the accumulator (P_{max}), when all the PCM has melted, is 90 Mpa, at which the Pentadecane obtains its highest thermodynamic efficiency (Falcão Carneiro and Gomes De Almeida, 2016). The pre-charge pressure (P_P) in the accumulator is 85 Mpa. The maximum gas volume in the accumulator is 10 L. The buoyancy magnification (M_b) is 8.5.

Step 4 : Calculate the ballast force (B_f) that the thermal buoyancy engine generates. Firstly, we input T_h and P_{max} into Eq. 17 (b) to calculate the unit volume of PCM in liquid phase (V_{PCM_L}), then we input T_l and P_{inner} into Eq. 17 (a) to calculate the unit volume of PCM in solid phase (V_{PCM_S}). Then, we use the Eq. (18) to calculate the ballast force, in this case, the B_f is 25 N.

$$B_f = \frac{V_{PCM_L} - V_{PCM_S}}{V_{PCM_S}} * V_{pcm} * \frac{M_b}{2} \quad \text{Eq. 18}$$

This force is significantly different and greater than typical ballast forces obtained with conventional thermal engines with the same amount of PCM.

4.3. The construction of the mathematical model

Once the design considerations of the UG have been determined, the next step is to construct the mathematical model to design the turbine for optimum energy extraction. The mathematical model is built to optimize λ_{design} and radius (R) based on the modified BEMT of Section 4.1. We show the procedure in the flowchart shown in Fig. 16.

The flowchart shows that the mathematical model consists of three loops. The core part or inner loop consists of step 4 to step 8. Rather than starting the description of the flowchart from top to bottom, we start from the inner (core) loop to the outside loop. This enables us to show how the more intricate part of the model connects to the outside considerations.

The innermost part is the core part from step 4 to step 8. After receiving a specific λ_{design}, design radius (R), the operating tip speed ratio ($\lambda_{operating}$) and the moving speed of the UG (V), this part will automatically design a turbine and analyse it based on the modified BEMT. We

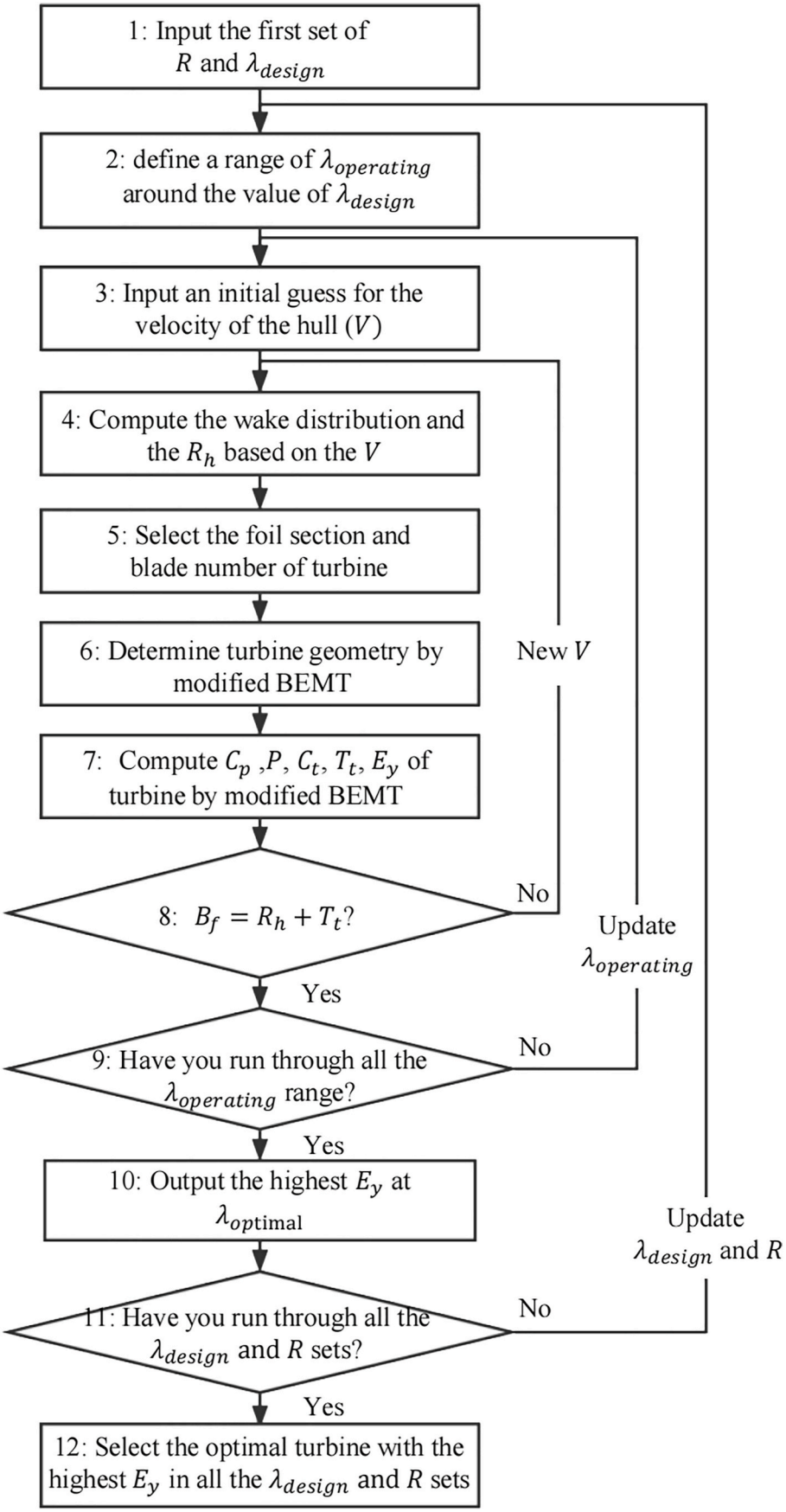

Fig. 16. The second part of the mathematical model.

describe in detail steps 4 to 8, as follows:

Step 4: Once step 4 receives a moving speed of the UG (V), it computes the wake distribution and hull resistance (R_h) based on V using Eq. (15) and Eq. (16).

Step 5: In this case, we select a NACA0015 foil section which is shown in Fig. 17. The C_L and C_D of this foil at different Re and α is input into the mathematical model in function form. The number of blades of the turbine is 3.

Step 6: Determine the turbine geometry. Once step 6 receives the λ_{design}, R, V, C_L, C_D and the wake distribution, it designs the turbine based on the modified BEMT. The detailed turbine design process is shown in the appendix of Fig. 24.

Step 7: Analyse the turbine based on the modified BEMT. Once step 7 received $\lambda_{operating}$, V, the wake distribution and the turbine geometry, the mathematical model will analyse the turbine's power coefficient (C_p), power (P), thrust coefficient (C_t), thrust (T_t), the energy yield of the turbine in each descent-ascent cycle (E_y) using

$$E_y = \frac{P * d_w * 2}{U_\infty} \quad \text{Eq. 19}$$

Step 8: Compute ballast force with Eq. (18). Check the force equilibrium state equation given by Eq. (20), such that:

$$B_f = T_t + R_h \quad \text{Eq. 20}$$

In summary, the first loop is implemented by step 4 and step 8 and it aims to find the real moving velocity of the system (V_{real}) that will satisfy the condition imposed by Eq. (20). We recall that results obtained from step 7 are the results at a certain velocity, but this velocity is not necessary the V_{real} of the whole energy yield mechanism which is currently unknown.

It is known that if an object is stable at a certain velocity, the external forces acting on the object balance each other. In this study, the whole mechanism consists of a turbine and a UG hull. For this system, the force equilibrium equation, Eq. (20), states that the sum of the resistance of the UG hull (R_h) and the turbine thrust (T_t) equals to the ballast force (B_f). Therefore, the inner loop will input different V values to find V_{real} that satisfies Eq. (20). We illustrate this procedure in Fig. 18.

The second loop is a counting loop implemented between step 2 and step 9. Step 3 and step 9 provide the mathematical model with possible operating tip speed ratios ($\lambda_{operating}$). This range is specified around the value of one specific λ_{design}. To specify the range of $\lambda_{operating}$, the lower limit is set as 25% of λ_{design} and the upper limit is set as 200% of λ_{design}. Although each turbine in this mathematical model has its own λ_{design}, the turbine does not necessarily reach the highest energy yield E_y when running at λ_{design}. Hence, the second loop uses the inner loop (step 3 to step 8) to find E_y for each $\lambda_{operating}$, and then we find the optimal E_y of a specific turbine.

Step 10, which is an intermediate step between the second loop and the outermost loop, obtains the optimal E_y among all $\lambda_{operating}$ of a specific turbine. This indicates the energy harvesting capability of a turbine. The $\lambda_{operating}$ with the optimal E_y is defined as $\lambda_{optimal}$.

Finally, the outermost counting loop implemented from step 1 and step 11 feeds the mathematical model different sets of λ_{design} and R, to explore the influence of λ_{design} and radius on the energy harvested (E_y). The aim is to find the values of λ_{design} and radius with the highest E_y. Since the optimal tip speed ratio for tidal turbines is around 4, and a very low λ_{design} can lead to oversized generators and power take-off mechanisms (Encarnacion et al., 2019), the range of λ_{design} is set from 2 to 6. Considering that a very small radius can lead the turbine to operate in a very strong wake, and a very large radius turbine is not foldable and is disproportionate with regards to the size of the UG hull. Hence, the radius ranges from 0.06 m to 0.15 m.

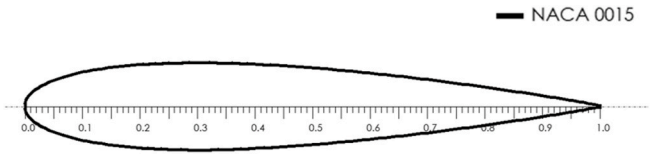

Fig. 17. The NACA0015 foil section.

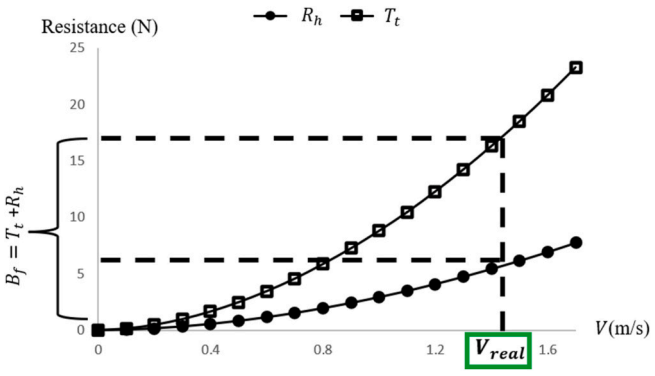

Fig. 18. The function of the first loop.

Finally, after finishing the calculation of all loops, the mathematical model will output the optimal turbine geometry with the highest E_y in all λ_{design} and R values.

5. The result of the mathematical model and the analysis

5.1. An optimal turbine

Once the flowchart of Fig. 19 is completed, the mathematical model will output the optimal E_y of turbines at different λ_{design} values and radiuses (R). This is shown in Fig. 19(a). The output corresponds to the turbine with the highest E_y which is the optimally designed turbine with the mathematical model. The geometry of this optimal turbine is shown in Fig. 19(b). We can observe the turbine has very wide chord. This is because the math model finds that a low TSR leads to the highest E_y.

5.2. Guidelines of mathematical model for turbine design

The result of Fig. 19(a) can be used to guide the design philosophy of the turbine in this study. The Fig. 19(a) shows that the E_y increases with increasing R and decreasing λ_{design}. Note that E_y increases as the radius increases because the larger radius will enable the turbine to capture more energy in competition with the hull. As shown in Fig. 20(a), during the entire energy harvesting process, the system is moving vertically in the water. We can simplify the hull into a virtual disk that absorbs the kinetic energy in the flow, similar to the virtual actuator disc of the turbine; because it blocks the incoming flow. Hence, a part of the kinetic energy in the incoming flow is captured by the hull and the rest part is captured by the turbine. We can regard the process as a competition between the hull and the turbine for kinetic energy because of their tandem relationship shown in the Fig. 20(b).

Also note that E_y decreases as λ_{design} because the Re number becomes smaller. We recall from Fig. 12, that at low Re, the hydrodynamic performance of the turbine deteriorates.

Fig. 21 shows Re computed at 0.9 r/R of the turbine blade length and how it changes with different R and λ_{design}. We chose 0.9 r/R, because in this section, the Re asymptotes to the highest in the entire blade. In fact, the typical Re distribution along the radius of the turbine blade is shown in Fig. 21(b). Furthermore, note that the blade element at 0.9 r/R contributes most to torque production.

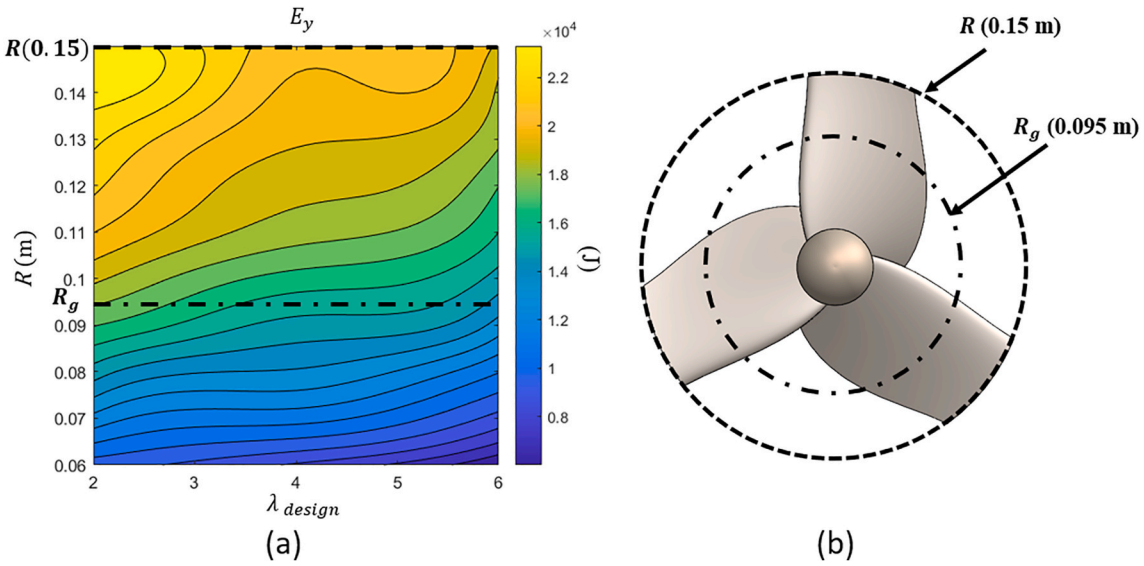

Fig. 19. a) The E_y of turbines with different sets of radius and λ_{design} b) the optimal turbine.

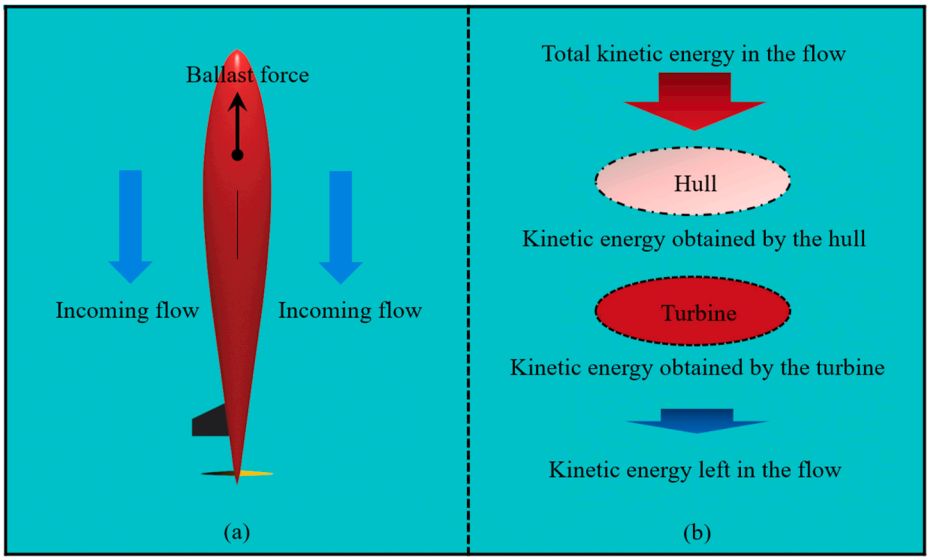

Fig. 20. a) the velocity of the flow b) the competition of kinetic energy.

Result from the mathematical model of a single case also shows that, a high C_p to C_t ratio (C_p/C_t) should be pursued for a turbine design in this energy harvesting mechanism. Fig. 22(a) shows E_y and Fig. 22(b) shows C_p, C_t and C_p/C_t versus $\lambda_{operating}$, for a turbine whose R is 0.15 m and whose λ_{design} is 4. Results are plotted over a range of $2 \leq \lambda_{operating} \leq 6$. The C_p/C_t curve in Fig. 22(b) shows the strongest correlations to E_y from Fig. 22(a). In fact, E_y and C_p/C_t reach their maximum value at $\lambda_{operating} = 3$, while C_p peaks at $\lambda_{operating} = 4$.

For this novel turbine, C_p/C_t reflects the pattern of E_y more accurately than C_p because the working principle of the turbine is fundamentally different to more traditional tidal turbines.

The C_p can no longer reflect the energy harvest ability because higher C_p may appear together with higher Ct, as shown in Fig. 22(b). A high Ct will decrease the moving velocity of the system which is also the incoming velocity of the turbine. Hence, it will also decrease the power and energy yield of the system. In contrast, when a high $C_p/\ C_t$ occurs, the turbine can yield a high C_p and avoid a low inflow speed caused by a high C_t. Hence, a high C_p/C_t leads to a high power and energy yield. Therefore, in the design process of a single turbine in this energy harvesting mechanism, the pursuit of higher C_p/C_t is the priority.

The multiple analysis of turbines with different sets of R and λ_{design} also shows the same conclusion. Fig. 23 shows the comparison between the C_p/C_t, the C_p, and the power output (P) in figure (a), (b), (c) respectively at different values of λ_{design} and R. Compared to the C_p and the P of the turbine, C_p/C_t shows a much more similar trend and stronger correlations with the E_y from Fig. 19(a). Hence, the highest C_p/C_t yields the highest E_y. This correlation contrasts the typical operation of a traditional turbine which pursues the highest C_p or P to maximise the harvested energy only, without any consideration of thrust.

Following this finding, the mathematical model will be further developed in future work. In the meantime, it should be pointed out that these conclusion are based on this specific UG hull in this case and they may change when choosing another hull with a higher C_t. A UG hull with a higher C_t may get more energy when competing with a turbine for energy, resulting in a decrease in the E_y of the turbine and influencing the optimal C_p/C_t of the mathematical model.

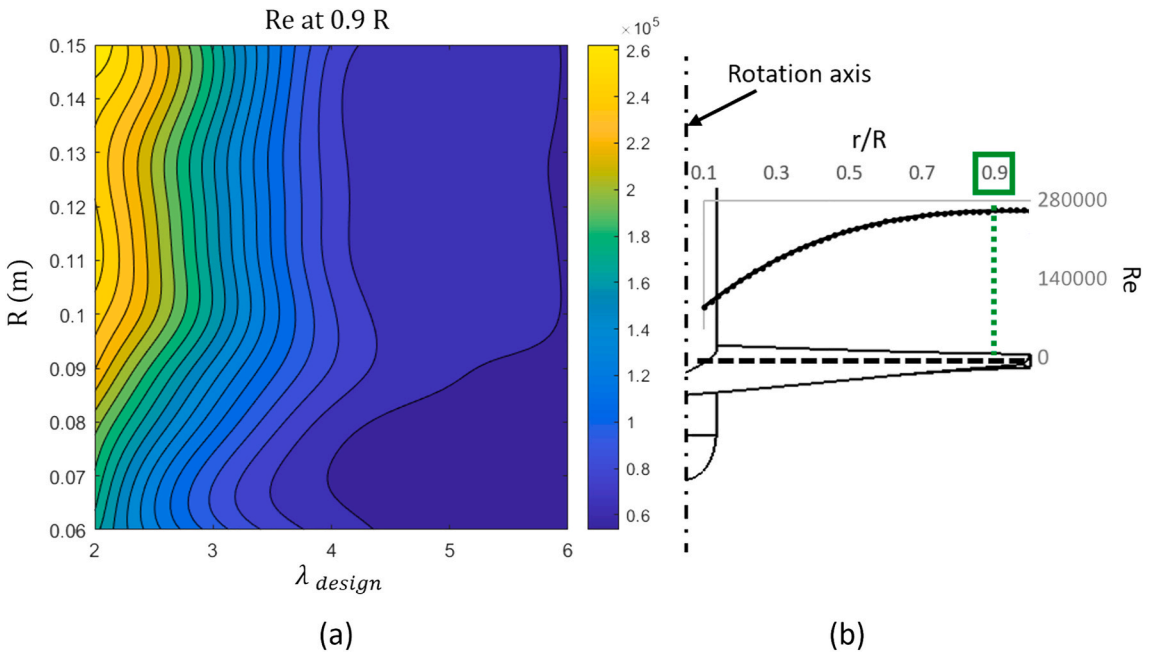

Fig. 21. a) The ***Re*** near the tip (0.9 r/R) of turbines of different sets of λ_{design} and R b) the typical ***Re*** distribution along the radius.

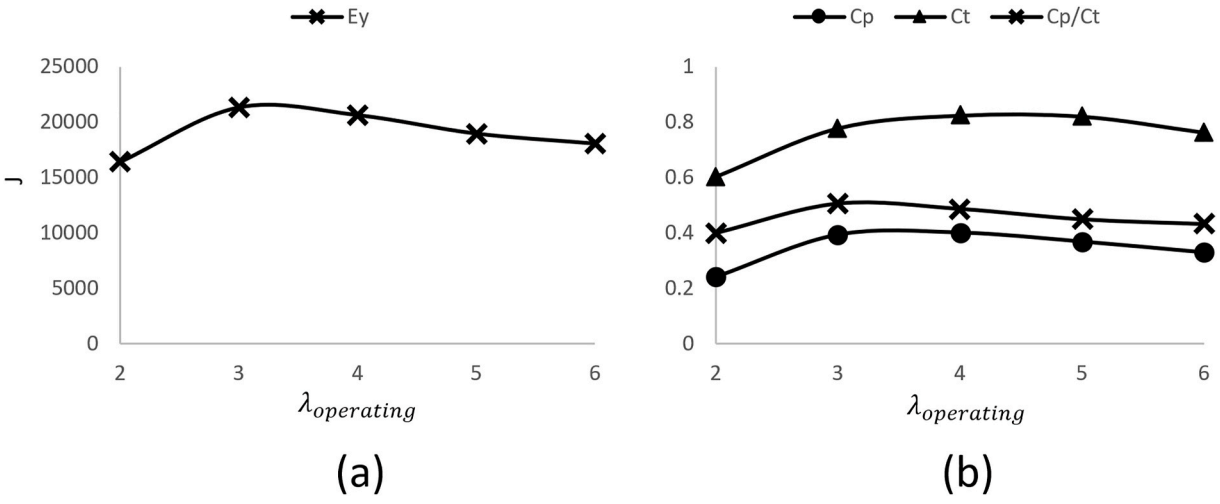

Fig. 22. a) E_y Vs $\lambda_{operating}$. b) C_p/C_t, C_p and C_t Vs $\lambda_{operating}$.

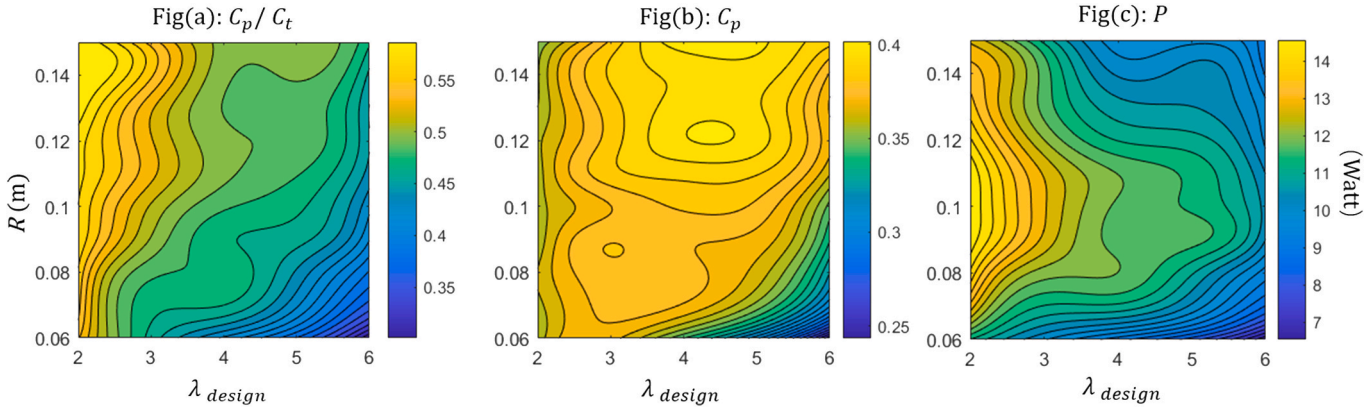

Fig. 23. ***a***) C_p/C_t, ***b***) C_p and c) ***P*** of turbines with different radius R and operating at different λ_{design}.

5.3. The energy harvesting capacity of the system with the optimal turbine

The mathematical model shows that this system can hydrodynamically harvest about 24.2 kJ of energy in one descent&ascent cycle in the energy harvesting mode when using the optimal turbine with 12 L (about 9.7 kg) of n-pentadecane. Considering that the power consumption of a typical UG of each descent&ascent cycle in gliding mode is about 6 kJ of energy (Davis et al., 2002a, Falcão Carneiro and Gomes De Almeida, 2018), it can be estimated that the energy harvested by the energy harvest system in 1 cycle can support the energy consumption of the UG in 4 cycles of the gliding mode.

The hydrodynamic energy conversion efficiency (η_h) of the mechanism is defined as the efficiency from the hydraulic energy output of the thermal buoyancy engine to the hydrodynamic energy output of the turbine. η_h can be calculated by Eq. (21).

$$\eta_h = \frac{E_y}{B_f * d_w * 2} \quad \text{Eq. 21}$$

As mentioned above, the ballast force of the thermal buoyancy engine (B_f) is 25 N, the working depth (d_w) of the buoyancy engine is 1000 m, the energy yield (E_y) in one descent&ascent cycle in the hydrodynamic level is 24.2 kJ; therefore, the η_h of the energy harvesting system is about 48%.

On the other hand, Wang reviewed the existing PCM-based energy harvesting mechanisms applied on UGs (Wang et al., 2020), showing the energy harvesting capability of SOLO-TREC, Slocum-TREC glider (Haldeman et al., 2015b) and OTEC-PCM(Wang et al., 2019). The proposed energy harvesting system has the potential to harvest more energy than the existing energy harvesting mechanisms with the same PCM loading. However, it is worth noticing that the energy yield in this study calculated from the hydrodynamic forces, which has not yet included the efficiency of the generator (varying from 60% to 90%) and the mechanical transmission losses of the system.

6. Conclusion

This work investigates a new-type of energy harvesting mechanism applied to a UG. The energy harvesting mechanism uses a novel thermal buoyancy engine and a turbine behind the hull to harvest energy. The following conclusions can be drawn:

1. A new-type of thermal buoyancy engine is developed, with patent applied. The new-type thermal buoyancy engine can fully use the pressure that the phase change material (PCM) can generate and amplify the ballast capacity to provide more kinetic energy to the turbine without increasing the mass of PCM.
2. The energy provided by the thermal engine is harvested by a turbine behind the hull of the UG. To have an energy efficient conversion of energy between the engine and the turbine, a mathematical model is developed based on the BEMT.
3. The mathematical model of BEMT was modified to consider the wake distribution behind the UG and the low operating Reynolds number. The mathematical model optimises the turbine in design tip speed ratio (λ_{design}) and radius (R). The mathematical model shows the trend that the energy yield of the turbine will increase with the decrease of λ_{design} and the increase of R. The model also shows the turbine should pursue higher C_p/C_t in the design process rather than pursuing higher C_p or P like the traditional turbine design. These observations can be used as a guideline for turbine design and can be used to further develop the mathematical model to design the optimal turbine.
4. The result of the mathematical model indicates that the hydrodynamic energy conversion efficiency of the energy harvesting mechanism is 48% when the working depth is 1000 m. The energy yield of 24.2 kJ in each cycle can support the energy consumption of the UG in 4 cycles in the gliding mode. This would allow the UG to be self-sustainable. This is a promising outlook for exploratory and rescue tasks in the ocean.

In future work, the hydrodynamic interaction between the hull and the turbine and the motion of the system in six degrees of freedom will be considered in a fully resolved CFD simulation. And further experimental investigations can be conducted to explore the challenges and opportunities to realise this technology.

CRediT authorship contribution statement

Hongbo Hou: Writing – review & editing, Data curation, numerical simulations, Conceptualization. **Abel Arredondo Galeana:** Writing – review & editing, numerical simulations. **Yang Song:** Writing – review & editing, system design, literature. **Gang Xu:** Reviewing, Writing – review & editing. **Yunxin Xu:** Numerical simulation, Formal analysis. **Weichao Shi:** Conceptualization, Methodology, Writing – review & editing, Supervision, Funding acquisition, All the authors here declare their contributions to the submitted paper. If any queries with regards to the contribution of the paper, please contact Dr Weichao Shi.

Declaration of competing interest

The authors declare the following financial interests/personal relationships which may be considered as potential competing interests: Weichao shi has patent #GB2597095 issued to WEICHAO SHI, HONGBO HOU, YUNXIN XU, MEHMET ALTAR. Hongbo Hou has patent #GB2597095 issued to WEICHAO SHI, HONGBO HOU, YUNXIN XU, MEHMET ALTAR. Yunxin Xu has patent #GB2597095 issued to WEICHAO SHI, HONGBO HOU, YUNXIN XU, MEHMET ALTAR.

Data availability

Data will be made available on request.

Acknowledgement

The funding support is received from the Royal Society, United Kingdom (Biomimetic improvement for the hydrodynamic performance of the enduring underwater glider, Ref: IEC\NSFC\201050). The authors would like to express their sincere gratitude for the fruitful discussions that happened in the research group, Applied Biomimetics Marine Hydrodynamics Group.

Appendix

The appendix shows the design part of modified BEMT, which is mentioned in section 4.1.

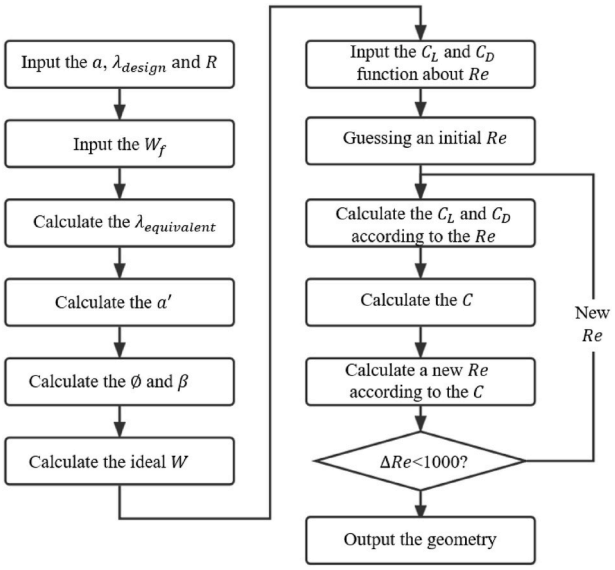

Fig. 24. The modified turbine design process based on the BEMT

References

Bangga, G., Hutomo, G., Syawitri, T.P., Kusumadewi, T.V., Oktavia, W., Sabila, A., Setiadi, H., Faisal, M., Hendranata, Y., Lastomo, D., Putra, L., Kristiadi, S.R., Bumi, I. M., 2018. Enhancing BEM Simulations of a Stalled Wind Turbine Using a 3D Correction Model.

Barthelmie, R.J., Hansen, K., Frandsen, S.T., Rathmann, O., Schepers, J., Schlez, W., Phillips, J., Rados, K., Zervos, A., Politis, E., 2009. Modelling and measuring flow and wind turbine wakes in large wind farms offshore. Wind Energy: An International Journal for Progress and Applications in Wind Power Conversion Technology 12, 431–444.

Buhl, M.L., 2005. New Empirical Relationship between Thrust Coefficient and Induction Factor for the Turbulent Windmill State.

Chao, Y., 2016. Autonomous underwater vehicles and sensors powered by ocean thermal energy. Oceans 1–4. Shanghai, 10-13 April 2016 2016.

Chaviaropoulos, P.K., Hansen, M., 2000. Investigating three-dimensional and rotational effects on wind turbine blades by means of a Quasi3D Navier-Stokes solver. Journal of Fluids Engineering-transactions of The Asme - J FLUID ENG 122.

Davis, R.E., Eriksen, C.C., Jones, C., 2002a. Autonomous Buoyancy-Driven Underwater Gliders.

Davis, R.E., Eriksen, C.C., Jones, C.P.J.T.T., Vehicles, A.O.A.U., 2002b. Autonomous Buoyancy-Driven Underwater Gliders. Taylor and Francis, London.

Deters, R., Ananda, G., Selig, M., 2014. Reynolds Number Effects on the Performance of Small-Scale Propellers.

Encarnacion, J.I., Johnstone, C., Ordonez-Sanchez, S., 2019. Design of a horizontal Axis tidal turbine for less energetic current velocity profiles. J. Mar. Sci. Eng. 7.

Eriksen, C.C., Osse, T.J., Light, R.D., Wen, T., Lehman, T.W., Sabin, P.L., Ballard, J.W., Chiodi, A.M., 2001. Seaglider: a long-range autonomous underwater vehicle for oceanographic research. IEEE J. Ocean. Eng. 26, 424–436.

Falcão Carneiro, J., Gomes De Almeida, F., 2016. Model of a thermal driven volumetric pump for energy harvesting in an underwater glider. Energy 112, 28–42.

Falcão Carneiro, J., Gomes De Almeida, F., 2018. Model and simulation of the energy retrieved by thermoelectric generators in an underwater glider. Energy Convers. Manag. 163, 38–49.

Haldeman, C.D., Schofield, O., Webb, D.C., Valdez, T.I., Jones, J.A., 2015. Implementation of energy harvesting system for powering thermal gliders for long duration ocean research. Oceans 1–5. MTS/IEEE Washington, 19-22 Oct. 2015 2015b.

Haldeman, C.D., Schofield, O., Webb, D.C., Valdez, T.I., Jones, J.A., 2015a. Implementation of Energy Harvesting System for Powering Thermal Gliders for Long Duration Ocean Research. OCEANS 2015-MTS/IEEE Washington, pp. 1–5. IEEE.

Javaid, M., Ovinis, M., Nagarajan, T., Hashim, F., 2014. Underwater gliders: a review. MATEC Web of Conferences 13, 02020.

Jones, C., Allsup, B., Decollibus, C., 2014. Slocum glider: expanding our understanding of the oceans. 2014 Oceans - St. John's 1–10, 14-19 Sept. 2014.

Khchine, Y.E., Sriti, M., 2017. Tip loss factor effects on aerodynamic performances of horizontal Axis wind turbine. Energy Proc. 118, 136–140.

Klintberg, L., Karlsson, M., Stenmark, L., Schweitz, J.-Å., Thornell, G., 2002. A large stroke, high force paraffin phase transition actuator. Sensor Actuator Phys. 96, 189–195.

Kong, Q., Ma, J., Xia, D., 2010. Numerical and experimental study of the phase change process for underwater glider propelled by ocean thermal energy. Renew. Energy 35, 771–779.

Li, L., 2013. Experimental Testing of Low Reynolds Number Airfoils for Unmanned Aerial Vehicles.

Liu, S., Janajreh, I., 2012. Development and application of an improved blade element momentum method model on horizontal axis wind turbines. International Journal of Energy and Environmental Engineering 3, 30.

Ma, Z., Wang, Y., Wang, S., Yang, Y., 2016. Ocean thermal energy harvesting with phase change material for underwater glider. Appl. Energy 178, 557–566.

Manwell, J.F., Mccowan, J., Rogers, A.L., 2006. Wind energy explained: theory, design and application. Wind Eng. 30, 169.

Manwell, J.F., Mcgowan, J.G., Rogers, A.L., 2010. Wind Energy Explained: Theory, Design and Application. John Wiley & Sons.

Schofield, O., Kohut, J., Aragon, D., Creed, L., Graver, J., Haldeman, C., Kerfoot, J., Roarty, H., Jones, C., Webb, D., Glenn, S., 2007. Slocum gliders: robust and ready. J. Field Robot. 24, 473–485.

Shen, W.Z., Mikkelsen, R., Sørensen, J., Bak, C., 2005. Tip loss correction for wind turbine computations. Wind Energy 8, 457–475.

Sherman, J., Davis, R.E., Owens, W.B., Valdes, J., 2001. The autonomous underwater glider "Spray. IEEE J. Ocean. Eng. 26, 437–446.

Shi, W., Atlar, M., Norman, R., Day, S., Aktas, B., 2019. Effect of waves on the leading-edge undulated tidal turbines. Renew. Energy 131, 435–447.

Shi, W., Hou, H., Xu, Y., Mehmet, A., 2022. A New Thermal Buoyancy Engine and its Control Method. Intellectual Property Office, GB2597095.

Sultania, A., Manuel, L., 2010. Extreme Loads on a Spar Buoy-Supported Floating Offshore Wind Turbine. 51st AIAA/ASME/ASCE/AHS/ASC Structures, Structural Dynamics, and Materials Conference 18th AIAA/ASME/AHS Adaptive Structures Conference 12th, p. 2738.

Wang, G., Yang, Y., Wang, S., Zhang, H., Wang, Y., 2019. Efficiency analysis and experimental validation of the ocean thermal energy conversion with phase change material for underwater vehicle. Appl. Energy 248, 475–488.

Wang, G., Yang, Y., Wang, S., 2020. Ocean thermal energy application technologies for unmanned underwater vehicles: a comprehensive review. Appl. Energy 278, 115752.

Webb, D.C., Simonetti, P.J., Jones, C.P., 2001. SLOCUM: an underwater glider propelled by environmental energy. IEEE J. Ocean. Eng. 26, 447–452.

Xue, D.-Y., Wu, Z.-L., Wang, Y.-H., Wang, S.-X., 2018. Coordinate control, motion optimization and sea experiment of a fleet of Petrel-II gliders. Chin. J. Mech. Eng. 31, 1–15.

Yang, Y., Wang, Y., Ma, Z., Wang, S., 2016. A thermal engine for underwater glider driven by ocean thermal energy. Appl. Therm. Eng. 99, 455–464.

Zhang, H.W., Wang, Y.H., Lian, Z.G., 2009. Application and improvement of the interlayer thermal engine powered by ocean thermal energy in an underwater glider. Asia-Pacific Power and Energy Engineering Conference 1–4, 27-31 March 2009 2009.